Capacitance characterization and current transport mechanism of ZnSnN$_2$ heterojunctions

View Online   Export Citation   CrossMark

Fan Ye,[a] Zi-Cheng Zhao, Cang-Shuang He, Jian-Lin Liang, Qian Gao, Yi-Zhu Xie, Dong-Ping Zhang, and Xing-Min Cai[a]

AFFILIATIONS

Key Laboratory of Optoelectronic Devices and Systems of Ministry of Education and Guangdong Province, Shenzhen Key Laboratory of Advanced Thin Films and Applications, College of Physics and Optoelectronic Engineering, and State Key Laboratory of Radio Frequency Heterogeneous Integration, Shenzhen University, Shenzhen 518060, China

[a]Authors to whom correspondence should be addressed: yefan@szu.edu.cn and caixm@szu.edu.cn

ABSTRACT

The trap and defect energy levels of ZnSnN$_2$ and the current transport mechanism of its heterojunctions are studied. A shallow energy level at 105 meV below the conduction band minimum (E$_c$) of ZnSnN$_2$ is detected and its possible origin is the intrinsic antisite defect of Sn$_{Zn}$ (Sn occupy the position of Zn in ZnSnN$_2$), besides the traps located at 0.67, 1.03 and 1.06 to 1.21 eV below E$_c$. The interface states of ZnSnN$_2$ heterojunctions form two discrete energy levels with one at E$_c$ + 0.05 eV and another at E$_c$ − 0.03 eV. The current of ZnSnN$_2$ heterojunctions is controlled by thermionic emission at relatively low bias voltage and limited by space charge at higher bias voltage. The barrier height of the heterojunctions is inhomogeneous, which obeys Gaussian distribution and possibly results from interface roughness.

14 December 2024 12:01:40

Developing solar cells based on Earth-abundant and eco-friendly semiconductors is essential in reducing the cost and expanding the application of photovoltaic (PV) technology.[1–7] ZnSnN$_2$ is considered as an eco-friendly solar cell absorber material that can meet terawatt-level energy demands at low cost.[4–6,8–21] Its advantages include a direct bandgap, high absorption coefficient ($\sim 10^5$ cm^{-1}), Earth-abundance of elements, non-toxicity of both the elements and the compound, and low cost. It belongs to the Zn-IV-N$_2$ (IV = Si, Ge, and Sn) family whose bandgap can match the solar spectrum.[10–13] ZnSnN$_2$ is also considered highly competent in photocatalytic and light emission device applications.[22,23]

Theoretical work shows that ZnSnN$_2$ is n-type conductive with electron density of 10^{19} cm^{-3} or even higher and with antisite defect of Sn$_{Zn}$ (Sn occupying the position of Zn) as the major donor.[4,5] In experiments, its electron density has been reduced[11,24–28] to around or below 10^{16} cm^{-3}. Devices of ZnSnN$_2$, including heterojunctions (HJ), HJ solar cells, Schottky diode, and Schottky barrier solar cells, have been studied.[6,29–32]

However, much still remains unknown about ZnSnN$_2$ and its devices. The energy levels of defects and traps in ZnSnN$_2$ and the current transport mechanism of its HJ have not been studied. In this paper, ZnSnN$_2$ HJ, with Cu$_2$O[7,33–37] as the p-type layer, is prepared with sputtering. The properties of ZnSnN$_2$ and the HJ are studied. The

defects and traps in ZnSnN$_2$ as well as the interface states and current transport mechanism of the HJ are revealed.

Both ZnSnN$_2$ and Cu$_2$O were prepared with magnetron sputtering. The base pressure of the vacuum chamber was 5.0×10^{-4} Pa. To measure the properties of ZnSnN$_2$ and Cu$_2$O, the substrates used were K9 glass and Si, which were ultrasonically cleaned in acetone, ethanol, and de-ionized water with the cleaning lasting for 15 min in each liquid. The rotational speed of the substrate holder was 0.6π rad/s. Before film deposition, the target was sputtered for 5 min to clean the target surface. An alloy target of Zn and Sn (99.999%) was used to deposit ZnSnN$_2$ and the atomic ratio of Zn to Sn is 6:1. Argon gas (99.99%) and nitrogen gas (99.999%) were introduced into the chamber. The flowrate of argon was eight standard cubic centimeters per minute (sccm) and that of nitrogen was 5 sccm. The working pressure was 5 Pa and the substrate temperature was 100 °C. Radio frequency (RF) sputtering was used and the power was 30 W. The deposition time was 4 h. A circular Cu plate (99.999%) was used as the target to deposit Cu$_2$O with direct current (DC) sputtering. The gases were Ar (99.99%) with a flow rate of 30 sccm and O$_2$ (99.999%) with a flow rate of 4 sccm. The working pressure was 0.6 Pa, the substrate temperature was 400 °C, and the deposition time was 1 h. The DC power was 50 W.

The fabrication of Cu$_2$O\ZnSnN$_2$ pn HJ (glass\ITO\Cu$_2$O\ ZnSnN$_2$\InSn) and the characterization methods of ZnSnN$_2$

and Cu$_2$O and the PV properties of the HJ are elaborated in the supplementary material. In forward bias, Cu$_2$O was connected to the positive electrode of the power source. The room temperature (RT) capacitance C vs voltage V (CV) curves of the devices at different frequencies were measured with an instrument (Victor, VC4092E LCR) equipped with a cryogenic platform (JANIS). The DC bias was from -1.00 to 1.00 V and the alternative current (AC) excitation source was 30 mV. The drive level capacitance profile (DLCP) and admittance spectroscopy (AS) curves were also measured with the same instrument. For RT DLCP measurements, the DC bias was from -0.25 to 0 V, the AC amplitude was from 0.015 to 0.135 V while the frequency was the same as that used for the RT CV curves. The zero-bias AS curves were measured from 180 to 380 K and the frequency was from 100 Hz to 1 MHz.

The dark temperature dependent IV or JV (I is the current and J is the current density) curves of the HJ were measured using a source measure unit instrument (Keithley 4200-SCS) and the temperature of the HJ was controlled by a constant temperature heating system (JF-956S, JFTOOLS, China).

The characterization results of ZnSnN$_2$ and Cu$_2$O and the PV properties of the HJ are presented in Figs. S1–S3 of the supplementary material. Figure 1(a) shows the RT CV curves measured at different frequencies, f. These CV curves are equivalent to metal/n-type semiconductor Schottky junctions.[38] Besides series resistance, the reverse-biased HJ capacitance C also results from those induced by interface states (C$_{IS}$), interface layer (C$_{IL}$), and space charge (C$_{SC}$). C$_{SC}$ equals $A_{sc}/(V_{bi}-V)^{1/2}$ where A$_{sc}$ is a constant, V$_{bi}$ is the built-in potential of the junction, and V is the applied voltage. The measured C here decreases with increasing frequency, mainly due to the decrease in response of the interface states with increasing frequency. In the

reverse-biased region, C is equivalent to C$_{IL}$ in series with two parallel branches, one is C$_{SC}$ and another is C$_{IS}$:[38] C^{-1} equals C$_{IL}^{-1}$ $+(C_{SC}+C_{IS})^{-1}$. If the interface layer is thin enough, C$_{IL}^{-1}$ is negligible and so

$$C = C_{SC} + C_{IS} = A_{SC}/(V_{bi}-V)^{1/2} + C_{IS}. \qquad (1)$$

The C^{-2} vs V curves are shown in Fig. S4 of the supplementary material, and it can be seen that they are not linear, implying that C$_{IS}$ cannot be ignored.

With A$_{sc}$, V$_{bi}$, and C$_{IS}$ as the fitting parameters, all the CV curves are fitted to Eq. (1) and the fitting results are presented in Table S1 of the supplementary material (the curves obtained at 900 and 500 Hz cannot be fitted and will be analyzed later). The successful fitting implies that the interfacial layer is thin enough and so C$_{IL}$ can be ignored. A$_{sc}$ and C$_{IS}$ are found to decrease while V$_{bi}$ increases with increase in frequency, in agreement with other results.[39] The fitted C$_{SC}^{-2}$ or $(C-C_{IS})^{-2}$ vs V curves are shown in Fig. 1(b). After C$_{IS}$ is removed, the C$_{SC}^{-2}$ vs V curves become linear for 1, 0.9, and 0.5 MHz due to the fact that deep levels respond less at higher frequencies. From the curve at 1 MHz, the built-in potential V$_{bi}$ is 0.59 V and the barrier height φ_b is calculated to be 0.67 V since the gap between the conduction band minimum E$_c$ and the Fermi level E$_f$ of ZnSnN$_2$ is 0.08 eV (see the supplementary material). The C$_{SC}^{-2}$ vs V curves at 100–9 kHz are still slightly curved (Fig. S5), implying the effect of deep levels or traps. The energy position and density of these deep levels are calculated[39–41] and listed in Table S2 of the supplementary material. Traps at 1.21, 1.14, and 1.09 eV below E$_c$ are found. Deep energy levels can deteriorate the performance of solar cells by trapping carriers to reduce short circuit current.
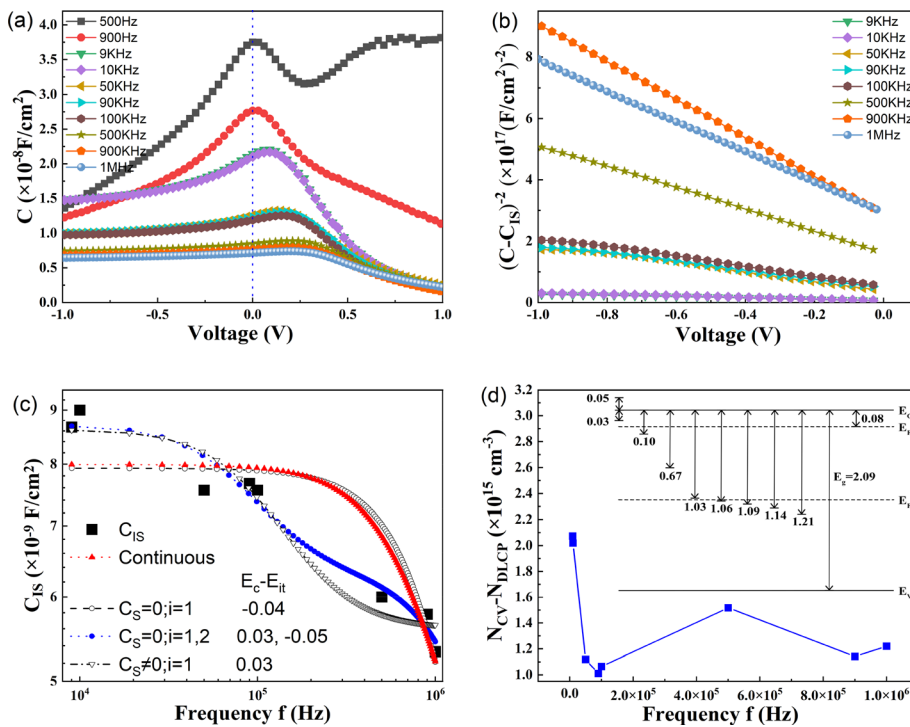

FIG. 1. (a) CV curves; (b) C$_{SC}^{-2}$ or $(C-C_{IS})^{-2}$ vs V curves; (c) C$_{IS}$ vs f data and the theoretical fitting; (d) N$_{it}$ vs f [Inset: the energy levels of interface states and defects or traps, the unit is eV; the bandgap energy of ZnSnN$_2$ is from Fig. S1(e), supplementary material].

The fitted C_{IS} data with four fitting models are shown in Fig. 1(c). For interface states forming continuous energy levels, C_{IS} equals $q^2 D_{it}(\omega\tau)^{-1} arctg(\omega\tau)$, where q is the unit charge, D_{it} and τ are the density and time constant of interface states, ω is the angular frequency (ω equals $2\pi f$).[42] A fitting to this model shows that D_{it} and τ are 4.99×10^{10} states $\cdot$ eV^{-1} $\cdot$ cm^{-2} and 2.40×10^{-7} s. However, the overlap between C_{IS} and the fitting curve is poor, possibly implying this model fails here. For interface states forming discrete levels, C_{IS}[42] is expressed as follows:

$$C_{IS} = C_S + \sum_1^m C_{it-i}/[1 + (2\pi f \tau_i)^2], \qquad (2)$$

where C_S is the semiconductor capacitance, m is the total number of discrete levels, i labels the ith level, τ_i and C_{it-i} are the time constant and the capacitance of the ith level. With $C_S = 0$, the fitting results show that the curve with two discrete levels overlaps with the C_{IS}-f data much better than that with one level. If C_S is used as a fitting parameter, only the model of m = 1 works. The fitting results are listed in Table S3 of the supplementary material. The density of interface states D_{it-i} and the corresponding interface states E_{it-i} are also calculated and listed in Table S3 since D_{it-i} equals C_{it-i}/q^2 while

$$\tau_i = f_i^{-1} = [v_{th}\sigma_n N_c]^{-1}\exp[(E_c - E_{it-i})/(kT)], \qquad (3)$$

where f_i is the ith level frequency, v_{th} is the thermal velocity of electrons, σ_n is the capture cross section, N_c is the density of states [$v_{th}\sigma_n N_c$ equals 2.10×10^6 Hz as shown later; for n-type semiconductors, the measurement frequency is too high for holes to follow and so the interface states detected are around the conduction band but not the valence band in Eq. (3)].[42] From the model with $C_S = 0$ and m = 2, E_c-$E_{it-1} = 0.03$ eV and this agrees with that obtained from $C_S \neq 0$ and m = 1. The model with $C_S = 0$ and m = 2 also shows that another energy level is 0.05 eV above E_c. This energy level needs further work though energy levels of impurities,[43] defects,[44] or interface states[45] above E_c are found in other semiconductors. Interface states are also harmful since they lead to interface recombination, which reduces the open circuit voltage.

The CV curves at 900 and 500 Hz cannot be fitted to Eq. (1) and the corresponding C^{-2}–V curves are shown in Fig. S6 of the supplementary material. These C^{-2}–V curves show concave-up curvature and can be divided into three linear sections due to interface states and deep levels. If we suppose that the interface states are in equilibrium with ZnSnN$_2$, N_D and V_{bi} of the first section can be calculated from the slope and horizontal intercept of section 1, while from section 2 and 3 the energy levels and the density of traps can be calculated (Fig. S6).[46,47] From the curve measured at 500 Hz, two trap energy levels at E_c-$E_{DL} = 0.67$ and 1.03 eV are found, while from that at 900 Hz E_c-$E_{DL} = 0.67$ and 1.06 eV are obtained. The deep energy levels and interface states are shown in the inset of Fig. 1(d).

From the CV curves, the depth profile of charge density, N_{CV}, which results from free carrier density as well as bulk and interfacial defect density can be obtained, while from drive level capacitance (DLC) the depth profile of the charge density, N_{DLCP}, which only results from the former two, can be obtained (Fig. S7 of the supplementary material).[48] The zero-bias difference between N_{CV} and N_{DLCP} at each frequency is exactly the total interface defect density N_{it} and is shown in Fig. 1(d). N_{it} varies with the frequency and is found to be around 1.5×10^{15} cm^{-3}. The possible peak at 0.5 MHz implies the

interface states energy level is 0.04 eV below E_c according to Eq. (3), roughly in agreement with Fig. 1(c). Below 90 KHz, N_{it} increases with a decrease in f in the measurement range. If we suppose that the minimum measurement frequency of 9 KHz is just the peak of N_{it}, the corresponding energy level of the interface states will be 0.14 eV below E_c according to Eq. (3). If the N_{it} peak is below 9 KHz, the corresponding energy level will be much deeper than 0.14 eV.

Figure 2(a) shows the capacitance C vs f obtained from AS. A step is seen in the curves and this suggests a discrete defect level is detected.[6,49] To obtain the activation energy E_a of this defect, the $-\omega dC/d\omega$ vs ω curves at each temperature are calculated, and from these curves, the angular frequency ω_0 corresponding to the maximum of the curve can be obtained. The relation between ω_0 and the activation energy E_a is that ω_0 equals $2\pi\nu_0 T^2\exp[-E_a/(kT)]$ or $2\pi f_0$, where ν_0 is the pre-exponential factor independent of temperature. Figure 2(b) shows the ω_0/T^2 vs 1000/T curve. ν_0 is calculated to be 23.34 Hz/K^2 and so $v_{th}\sigma_n N_c$ equals 2.10×10^6 Hz according to Eq. (3). E_a is found to be 105 meV (or 0.10 eV). The integrated total density based on Gaussian distribution, N_t, is 1.66×10^{16} cm^{-3} [Fig. 2(c)].

There are three possible origins for this energy level: from Cu$_2$O, the interface states, or ZnSnN$_2$. It is known that the preparation methods have an influence on E_a of defects. In Ref. 35, the E_a values for Cu$_2$O deposited at 600 and 1070 K are 0.23 and 0.19 eV. The preparation methods of our Cu$_2$O are very similar to that except that the substrate temperature used is 673 K here. The E_a of Cu$_2$O here should be between 0.23 and 0.19 eV, larger than 105 meV. This level also cannot result from interface states since the energy levels of interface states are at E_c−0.03 eV or E_c+0.05 eV in Fig. 1(c) while one around E_c−0.04 eV and another deeper than E_c−0.14 eV are estimated in Fig. 1(d). Therefore, this level can only come from ZnSnN$_2$ and the possible origin is the antisite defect of Sn$_{Zn}$ since in ZnSnN$_2$, Sn$_{Zn}$ is the major donor having the lowest formation energy.

Figure 2(d) shows the experimental and fitted Nyquist spectra of the HJ and the inset shows the equivalent circuit used for fitting.[6] The HJ can be fitted with one resistance R_s in series with two parallel branches: one is the parallel resistance R_p and another is the constant phase element (CPE, which includes two parameters: CPE-P and CPE-T—CPE-P is within 0–1, CPE-P = 1 implies that it is a pure capacitor while CPE-P = 0 implies it is a pure resistance). The fitted R_s, R_p, CPE-P, and CPE-T are 30.18 Ω, 3199 Ω, 0.81, and 1.24×10^{-8}, respectively. The time constant of the CPE, which equals $[R_p \times (CPE - T)]^{1/(CPE-P)}$, is calculated to be 3.97×10^{-6} s. This is larger than that of the interface states (Table S3), suggesting that interface states have a weak influence on the current transport. The existence of CPE also implies interface roughness.

The dark JV curves at different temperatures are shown in Fig. 3(a). As the temperature increases, J increases. In the forward double log JV curves [Fig. 3(b)], the slope of the curves at lower bias (<1 V) is close to 1, indicating Ohmic conduction and the current is controlled by the junction while the slope approaches 2 under high bias voltage, indicating that space charge limited current (SCLC) gradually becomes dominant.

The possible transport models of HJ[50–53] currents include tunneling, diffusion, generation/recombination in the space charge region, and thermionic emission (TE). In these models, the forward bias current density J equals $J_s\{\exp[A(T)V]-1\}$, where J_s is the saturation
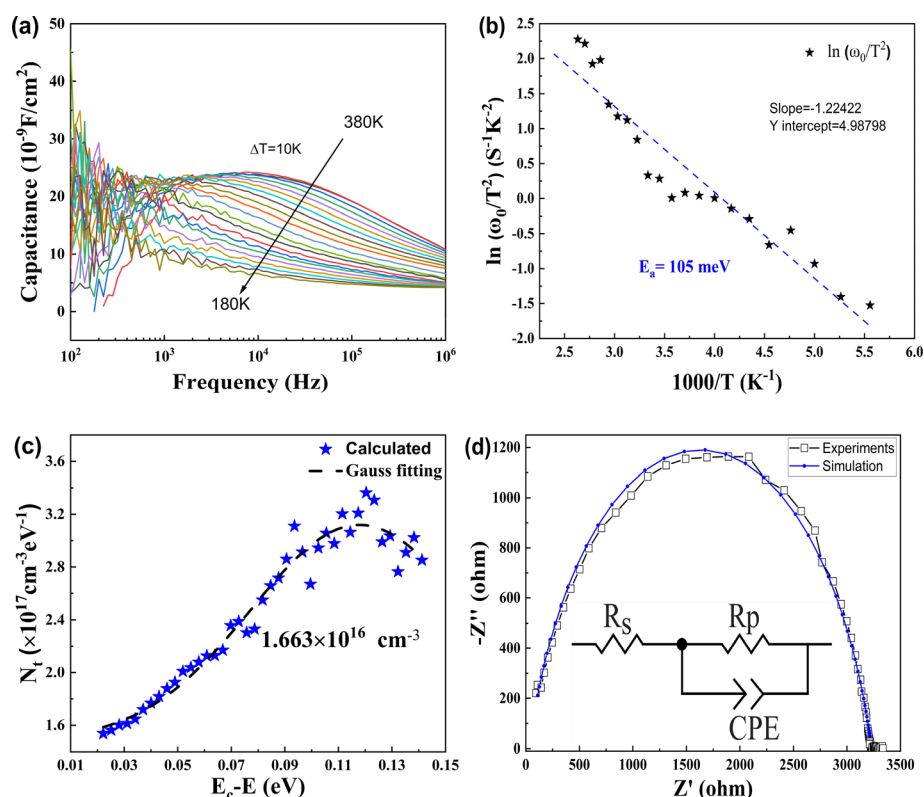
FIG. 2. (a) The admittance spectra of the HJ. (b) The Arrhenius plot of $\ln(\omega_0/T^2)$ vs 1000/T. (c) The integrated density of the defect or trap. (d) The impedance spectrum of the HJ.
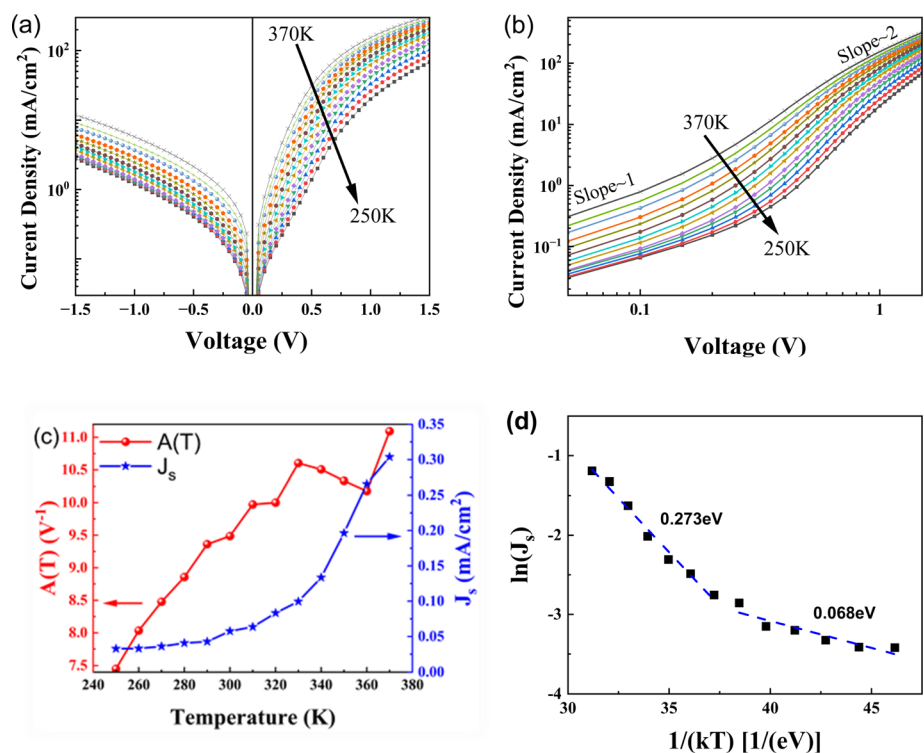

FIG. 3. (a) J~V curves at 250–370 K. (b) Forward bias logarithmic J~ logarithmic V curves. (c) A(T) and J_s vs T. (d) ln (J_s) vs 1/(kT).

current density, A(T) is the exponential factor. When the applied voltage is over $3kT/q$, J just equals $J_s\exp[A(T)V]$. J_s and A(T) can then be obtained from the linear region of the lnJ vs V plot, as shown in Fig. 3(c). It is seen that A(T) is not a constant in the whole temperature range and this excludes the possibility of tunneling. In addition, if the current is due to diffusion or generation/recombination in the space charge region, the activation energy from the $\ln J_s$ vs $1/(kT)$ curve would be the bandgap or half the bandgap. However, the activation energy from the $\ln J_s$ vs $1/(kT)$ curves is just about 0.273/0.068 eV [Fig. 3(d)], far smaller than that of Cu_2O or $ZnSnN_2$. Therefore, the current at low bias is controlled by TE.

According to the TE model, the JV relation is given by

$$J = J_s\{\exp[q(V - JR_s)/(nkT)] - 1\} + J_{sh}, \quad (4)$$

where

$$J_s = A^{**}T^2\exp(-q\varphi_b/kT). \quad (5)$$

J_{sh} equals $(V-IR_s)/R_{sh}$, R_s is the resistance in series with the diode, R_{sh} is a resistance in parallel to R_s and the diode, A^{**} is the effective Richardson coefficient [A^{**} of $ZnSnN_2$ is 14.40 (Ref. 29) $A\cdot cm^{-2}\cdot K^{-2}$], n is the ideality factor, φ_b is the barrier height, and the other symbols are consistent with the previous equations. With φ_b, n, R_s, and R_{sh} as the fitting parameters, the current density in the junction-controlled region (below 1 V) can be fitted to Eq. (4) and the fitting results are presented in Figs. 4(a) and 4(b). The barrier height φ_b increases with temperature increase while the ideality factor n is over 1 and decreases with temperature increase, implying barrier height inhomogeneity (BHI).[54–56] The series resistance R_s decreases with temperature decrease due to carrier freezing-out while R_{sh} increases with temperature increase.[50]

From Eq. (5), the following equation can be obtained:

$$\ln(J_s/T^2) = \ln(A^{**}) - q\varphi_b/(kT). \quad (6)$$

Equation (6) shows that $\ln(J_s/T^2)$ vs $q/(kT)$ curves (the Richardson plot) will be linear. In the Richardson plot in Fig. 4(c), the linearity in the whole temperature range is not good. φ_b and A^{**} are 0.12/0.26 V and $3.69\times10^{-8}/1.28\times10^{-5}$ $A\cdot cm^{-2}\cdot K^{-2}$ in the low/high temperature range. The obtained A^{**} is much smaller than the theoretical value, also suggesting possible BHI.[54–56] With the presence of BHI, the relations between φ_b, n, and T are as follows:[54,55]

$$\varphi_b = \overline{\varphi_{b0}} - q\sigma_0^2/(2kT), \quad (7)$$
$$n^{-1} - 1 = -\rho_2 + q\rho_3/(2kT), \quad (8)$$

where $\overline{\varphi_{b0}}$ and σ_0 are standard barrier height and deviation at zero-bias while ρ_2 and ρ_3 are two coefficients. Figure 4(d) shows the plots of φ_b and $n^{-1}-1$ vs $q/(2kT)$. From Eq. (7), $\overline{\varphi_{b0}}$ and σ_0 are obtained to be 1.05 and 0.15 V while from Eq. (8), ρ_2 and ρ_3 are 0.44 and -0.01 V. Since φ_b is related to temperature according to Eq. (7), Eq. (6) can now be turned into the modified Richardson relationship given by

$$\ln(J_s/T^2) - q^2\sigma_0^2/(2k^2T^2) = \ln(A^{**}) - q\overline{\varphi_{b0}}/(kT). \quad (9)$$

Equation (9) shows that $\ln(J_s/T^2) - q^2\sigma_0^2/(2k^2T^2)$ vs $q/(kT)$ will be linear. The modified Richardson plot is presented in Fig. 4(c) and good linearity is observed in the whole temperature range. The calculated $\overline{\varphi_{b0}}$ is 1.05 V, in agreement with that obtained from Fig. 4(d) while A^{**} is 14.41 $A\cdot cm^{-2}\cdot K^{-2}$, very close to the theoretical data. Therefore, the temperature dependence of barrier height can be explained by BHI, which obeys the Gaussian distribution and possibly results from interface roughness. With the presence of BHI, the open circuit voltage will be much smaller than the barrier height extracted from IV curves and factors resulting in BHI should try to be avoided during HJ preparation.

In summary, $ZnSnN_2$ HJ was prepared and studied. CV curves show that the capacitance is affected by interface states and trap energy levels. The interface states form two discrete energy levels with one
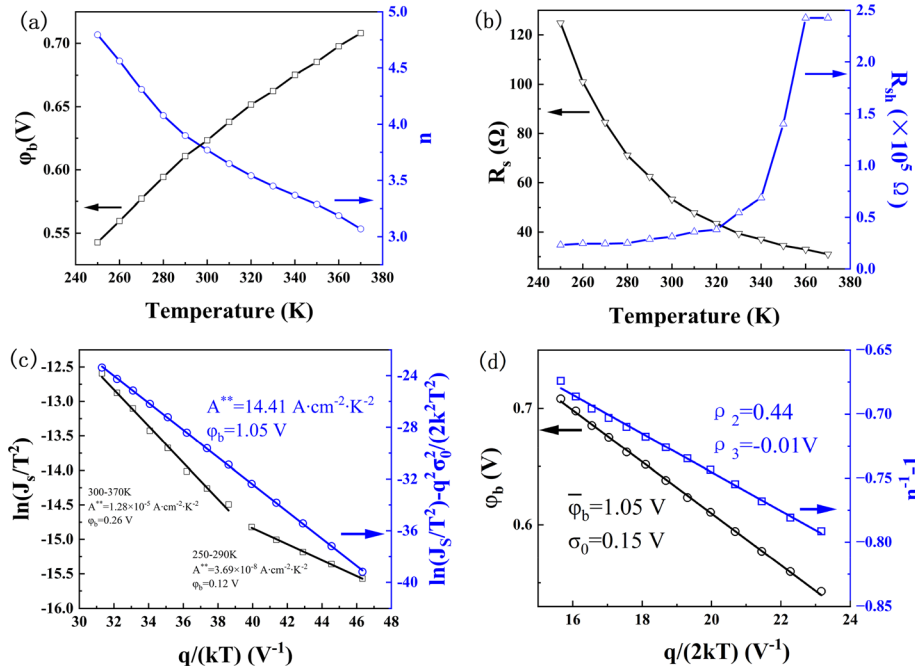

FIG. 4. (a) φ_b and n vs temperature. (b) R_s and R_{sh} vs temperature. (c) The Richardson plot and the modified one. (d) φ_b and $n^{-1}-1$ vs $q/(2kT)$ plot.

below and one above E_c of $ZnSnN_2$. The former is also confirmed by the zero-bias difference of the charge profile. The deep energy levels are located at 0.67, 1.03 and 1.06 to 1.21 eV below E_c of $ZnSnN_2$. A shallow energy level at 105 meV below E_c is detected and the possible origin is the intrinsic antisite defect of Sn_{Zn}. JV curves show that the dominant transport mechanism is TE at lower voltage. The extracted barrier height is inhomogeneous and the possible origin is interface roughness as revealed by impedance spectra.

See the supplementary material for the following content: Methods about preparing the $Cu_2O\backslash ZnSnN_2$ heterojunctions; Characterization methods of $ZnSnN_2$ and Cu_2O; Characterizations of the photovoltaic properties of the HJ; The XRD spectra, Raman scattering spectra and Tauc plots of $ZnSnN_2$ and Cu_2O; SEM images and Hall effect measurements; The illuminated JV curve, EQE spectrum and $[E\times ln(1-EQE)]^2$ vs E plot of the HJ; The reverse-biased C^{-2}-V curves; The fitting results based on $C = C_{SC} + C_{IS}$; The fitted C_{sc}^{-2} or $(C - C_{IS})^{-2}$ vs V curves for 100, 90, 50, 10, and 9 KHz and the calculation about the energy levels and the density; The fitting results based on Eq. (2); The C^{-2} vs V curves for 900 and 500 Hz and the calculation about the energy levels and the density; The calculation about N_{CV} and N_{DLCP}.

AUTHOR DECLARATIONS
Conflict of Interest
The authors have no conflicts to disclose.

Author Contributions
Fan Ye: Conceptualization (equal); Data curation (equal); Formal analysis (equal); Funding acquisition (equal); Investigation (equal); Methodology (equal); Project administration (equal); Resources (equal); Software (equal); Supervision (equal); Validation (equal); Visualization (equal); Writing – original draft (equal); Writing – review & editing (equal). **Zi-Cheng Zhao:** Data curation (equal); Formal analysis (equal); Investigation (equal); Methodology (equal); Software (equal); Writing – original draft (supporting). **Cang-Shuang He:** Formal analysis (supporting); Visualization (supporting). **Jian-Lin Liang:** Data curation (supporting); Formal analysis (supporting). **Qian Gao:** Data curation (supporting); Visualization (supporting). **Yi-Zhu Xie:** Resources (supporting). **Dong-Ping Zhang:** Resources (supporting). **Xing-Min Cai:** Conceptualization (equal); Data curation (equal); Formal analysis (equal); Investigation (equal); Writing – original draft (equal); Writing – review & editing (equal).

DATA AVAILABILITY
The data that support the findings of this study are available from the corresponding author upon reasonable request.

REFERENCES

[1]O. Surucu, G. Surucu, N. M. Gasanly, M. Parlak, and M. Isik, "Exploring temperature-dependent bandgap and urbach energies in CdTe thin films for optoelectronic applications," Mater. Lett. **373**, 137078 (2024).

[2]M. Isik and N. M. Gasanly, "Identification of shallow trap centers in InSe single crystals and investigation of their distribution: A thermally stimulated current spectroscopy," Opt. Mater. **156**, 116011 (2024).

[3]A. Doğan, A. Karatay, M. Isik, E. A. Yıldız, N. M. Gasanly, and A. Elmali, "Revealing the effects of defect states on the nonlinear absorption properties of the TlInSSe and $Tl_2In_2S_3Se$ crystals in near-infrared optical limiting applications," Cryst. Growth Des. **24**(17), 6981–6990 (2024).

[4]S. Y. Chen, P. Narang, H. A. Atwater, and L. W. Wang, "Phase stability and defect physics of a ternary $ZnSnN_2$ semiconductor: First principles insights," Adv. Mater. **26**(2), 311–315 (2014).

[5]J. Pan, J. Cordell, G. J. Tucker, A. C. Tamboli, A. Zakutayev, and S. Lany, "Interplay between composition, electronic structure, disorder, and doping due to dual sublattice mixing in nonequilibrium synthesis of $ZnSnN_2$: O," Adv. Mater. **31**(11), 1807406 (2019).

[6]F. Ye, C. S. He, T. Wu, S. Chen, Z. H. Su, X. H. Zhang, X. M. Cai, and G. X. Liang, "Sputtering deposited and energy band matched $ZnSnN_2$ buffer layers for highly efficient Cd-free Cu_2ZnSnS_4 solar cells," Adv. Funct. Mater. **34**(38), 2402762 (2024).

[7]Z. G. Zang, "Efficiency enhancement of ZnO/Cu_2O solar cells with well oriented and micrometer grain sized Cu_2O films," Appl. Phys. Lett. **112**(4), 042106 (2018).

[8]A. Nezhdanov, A. Skrylev, D. Shestakov, D. Usanov, D. Fukina, A. Malyshev, G. De Filpo, and A. Mashin, "Mixed phase $ZnSnN_2$ thin films for solar energy applications: Insight into optical and electrical properties," Opt. Mater. **144**, 114335 (2023).

[9]A. Laidouci, Mamta, V. N. Singh, P. K. Dakua, and D. K. Panda, "Performance evaluation of $ZnSnN_2$ solar cells with Si back surface field using SCAPS-1D: A theoretical study," Heliyon **9**(10), e20601 (2023).

[10]J. J. Cordell, S. Lany, and M. B. Tellekamp, "Comparing the influence of cation order and composition in simulated $Zn(Sn, Ge)N_2$ on structure, elastic moduli, and polarization for solid state lighting," J. Appl. Phys. **135**(7), 075001 (2024).

[11]J. W. Choi, J. Kim, S. R. Pae, J. Kim, C. G. Kim, H. Lee, S. Ji, S. W. Nam, Y. K. Lee, and B. Shin, "Oxidation-resistant amorphous zinc tin nitride films with tunable optical and electrical properties," Chem. Mater. **34**(15), 6802–6808 (2022).

[12]M. Ogura, D. Han, M. M. Pointner, L. S. Junkers, S. S. Rudel, W. Schnick, and H. Ebert, "Electronic properties of semiconducting $Zn(Si,Ge,Sn)N_2$ alloys," Phys. Rev. Mater. **5**(2), 024601 (2021).

[13]A. Laidouci, P. K. Dakua, D. K. Panda, and S. Kashyap, "Investigating the potential of earth-abundant $ZnSn_xGe_{1-x}N_2$ alloys for quantum well solar cells," Micro Nanostructures **184**, 207696 (2023).

[14]T. R. Paudel and W. R. L. Lambrecht, "First-principles study of phonons and related ground-state properties and spectra in Zn-IV-N_2 compounds," Phys. Rev. B **78**(11), 115204 (2008).

[15]L. Lahourcade, N. C. Coronel, K. T. Delaney, S. K. Shukla, N. A. Spaldin, and H. A. Atwater, "Structural and optoelectronic characterization of RF sputtered $ZnSnN_2$," Adv. Mater. **25**(18), 2562–2566 (2013).

[16]P. C. Quayle, K. L. He, J. Shan, and K. Kash, "Synthesis, lattice structure, and band gap of $ZnSnN_2$," MRS Commun. **3**(3), 135–138 (2013).

[17]K. K. Chinnakutti, V. Panneerselvam, and S. T. Salammal, "Ba-acceptor doping in $ZnSnN_2$ by reactive RF magnetron sputtering:(002) faceted Ba-$ZnSnN_2$ films," J. Alloys Compd. **855**, 157380 (2021).

[18]P. C. Quayle, E. W. Blanton, A. Punya, G. T. Junno, K. L. He, L. Han, H. P. Zhao, J. Shan, W. R. L. Lambrecht, and K. Kash, "Charge-neutral disorder and polytypes in heterovalent wurtzite-based ternary semiconductors: The importance of the octet rule," Phys. Rev. B **91**(20), 205207 (2015).

[19]B. B. Dumre, R. J. Nelson, R. E. Irving, R. J. Ellingson, and S. V. Khare, "Trends in opto-electronic properties of $Mg_xZn_{1-x}SnN_2$ using first principles methods," Mater. Chem. Phys. **294**, 126995 (2023).

[20]A. Aissat, L. Chenini, A. Laidouci, S. Nacer, and J. P. Vilcot, "Improvement in the efficiency of solar cells based on the $ZnSnN_2/Si$ structure," Mater. Sci. Eng. B **300**, 117071 (2024).

[21]A. Laidouci, A. Aissat, and J. P. Vilcot, "Numerical study of solar cells based on $ZnSnN_2$ structure," Sol. Energy **211**, 237–243 (2020).

[22]M. R. Karim and H. P. Zhao, "Design of InGaN-$ZnSnN_2$ quantum wells for high-efficiency amber light emitting diodes," J. Appl. Phys. **124**(3), 034303 (2018).

[23] D. Q. Fang, X. Chen, P. F. Gao, Y. Zhang, and S. L. Zhang, "Mono- and bilayer ZnSnN$_2$ sheets for visible-light photocatalysis: First-principles predictions," J. Phys. Chem. C **121**(46), 26063–26068 (2017).

[24] X. J. Wu, F. Z. Meng, D. L. Chu, M. C. Yao, K. Guan, D. D. Zhang, and J. Meng, "Carrier tuning in ZnSnN$_2$ by forming amorphous and microcrystalline phases," Inorg. Chem. **58**(13), 8480–8485 (2019).

[25] F. Ye, Z. Ke, L. H. Yuan, R. T. Hong, D. P. Zhang, P. Fan, and X. M. Cai, "Electrical and optical properties of nanocrystalline ZnSnN$_2$," Thin Solid Films **772**, 139804 (2023).

[26] A. N. Fioretti, A. Stokes, M. R. Young, B. Gorman, E. S. Toberer, A. C. Tamboli, and A. Zakutayev, "Effects of hydrogen on acceptor activation in ternary nitride semiconductors," Adv. Electron. Mater. **3**(3), 1600544 (2017).

[27] F. Ye, Q. Q. Chen, X. M. Cai, Y. Z. Xie, X. F. Ma, K. Vaithinathan, D. P. Zhang, P. Fan, and V. A. L. Roy, "Improving the chemical potential of nitrogen to tune the electron density and mobility of ZnSnN$_2$," J. Mater. Chem. C **8**(13), 4314–4320 (2020).

[28] J. Y. Ren, L. Y. Liang, X. H. Liu, and H. T. Cao, "Physical properties of Zn-Sn-N films governed by the Zn/(Zn+Sn) ratio," J. Vac. Sci. Technol. A **41**(3), 033406 (2023).

[29] F. Ye, R. T. Hong, C. S. He, Z. C. Zhao, Y. Z. Xie, D. P. Zhang, F. Wang, J. W. Li, and X. M. Cai, "ZnSnN$_2$ Schottky barrier solar cells," Mater. Sci. Eng. B **300**, 117097 (2024).

[30] R. F. Qin, H. T. Cao, L. Y. Liang, Y. F. Xie, F. Zhuge, H. L. Zhang, J. H. Gao, K. Javaid, C. C. Liu, and W. Z. Sun, "Semiconducting ZnSnN$_2$ thin films for Si/ZnSnN$_2$ p-n junctions," Appl. Phys. Lett. **108**(14), 142104 (2016).

[31] K. Javaid, W. H. Wu, J. Wang, J. F. Fang, H. L. Zhang, J. H. Gao, F. Zhuge, L. Y. Liang, and H. T. Cao, "Band offset engineering in ZnSnN$_2$-based heterojunction for low-cost solar cells," ACS Photonics **5**(6), 2094–2099 (2018).

[32] F. Ye, R. T. Hong, Y. B. Qiu, Y. Z. Xie, D. P. Zhang, P. Fan, and X. M. Cai, "Nanocrystalline ZnSnN$_2$ prepared by reactive sputtering, its Schottky diodes and heterojunction solar cells," Nanomaterials **13**(1), 178 (2022).

[33] B. K. Meyer, A. Polity, D. Reppin, M. Becker, P. Hering, P. J. Klar, T. Sander, C. Reindl, J. Benz, M. Eickhoff, C. Heiliger, M. Heinemann, J. Bläsing, A. Krost, S. Shokovets, C. Müller, and C. Ronning, "Binary copper oxide semiconductors: From materials towards devices," Phys. Status Solidi B **249**(8), 1487–1509 (2012).

[34] R. C. Wang and C. H. Li, "Cu, Cu-Cu$_2$O core-shell, and hollow Cu$_2$O nanodendrites: Structural evolution and reverse surface-enhanced Raman scattering," Acta Mater. **59**(2), 822–829 (2011).

[35] Y. S. Lee, M. T. Winkler, S. C. Siah, R. Brandt, and T. Buonassisi, "Hall mobility of cuprous oxide thin films deposited by reactive direct-current magnetron sputtering," Appl. Phys. Lett. **98**(19), 192115 (2011).

[36] A. El-Shaer, N. Darwesh, M. A. Habib, and M. Abdelfatah, "Doping of nanostructured Cu$_2$O films to improve physical and photoelectrochemical properties as a step forward for optoelectronics applications," Opt. Mater. **148**, 114849 (2024).

[37] A. Lakshmanan, Z. C. Alex, and S. R. Meher, "N-type In (or Al) doped Cu$_2$O thin films by magnetron sputtering," Eur. Phys. J. Plus **139**, 62 (2024).

[38] P. K. Vasudev, B. L. Mattes, E. Pietras, and R. H. Bube, "Excess capacitance and non-ideal Schottky barriers on GaAs," Solid-State Electron. **19**(7), 557–559 (1976).

[39] A. M. Goodman, "Metal-semiconductor barrier height measurement by the differential capacitance method-one carrier system," J. Appl. Phys. **34**(2), 329–338 (1963).

[40] G. I. Roberts and C. R. Crowell, "Capacitance energy level spectroscopy of deep-lying semiconductor impurities using Schottky barriers," J. Appl. Phys. **41**(4), 1767–1776 (1970).

[41] G. I. Roberts and C. R. Crowell, "Capacitive effects of Au and Cu impurity levels in Pt-n type Si Schottky barriers," Solid-State Electron. **16**(1), 29–38 (1973).

[42] E. H. Nicollian and A. Goetzberger, "The Si-SiO$_2$ interface-electrical properties as determined by the metal-insulator silicon conductance technique," Bell Syst. Tech. J. **46**(6), 1055–1133 (1967).

[43] D. G. Zhao, D. S. Jiang, J. J. Zhu, Z. S. Liu, H. Wang, S. M. Zhang, Y. T. Wang, and H. Yang, "Role of edge dislocation and Si impurity in linking the blue luminescence and yellow luminescence in n-type GaN films," Appl. Phys. Lett. **95**(4), 041901 (2009).

[44] A. D. Prins, M. K. Lewis, Z. L. Bushell, S. J. Sweeney, S. Liu, and Y.-H. Zhang, "Evidence for a defect level above the conduction band edge of InAs/InAsSb type-II superlattices for applications in efficient infrared photodetectors," Appl. Phys. Lett. **106**(17), 171111 (2015).

[45] W. R. Anderson, R. G. Wheeler, and T. P. Ma, "Observation of interface traps in the silicon conduction band at the (100)Si/SiO$_2$ interface at 4.2 K," Appl. Phys. Lett. **61**(9), 1107–1109 (1992).

[46] P. Cova and A. Singh, "Temperature dependence of I-V and C-V characteristics of Ni/n-CdF$_2$ Schottky barrier type diodes," Solid-State Electron. **33**(1), 11–19 (1990).

[47] I. Balberg, "Relation between distribution of states and the space-charge-region capacitance in semiconductors," J. Appl. Phys. **58**(7), 2603–2616 (1985).

[48] J. T. Heath, J. D. Cohen, and W. N. Shafarman, "Bulk and metastable defects in CuIn$_{1-x}$Ga$_x$Se$_2$ thin films using drive-level capacitance profiling," J. Appl. Phys. **95**(3), 1000–1010 (2004).

[49] T. Walter, R. Herberholz, C. Müller, and H. W. Schock, "Determination of defect distributions from admittance measurements and application to Cu(In, Ga)Se$_2$ based heterojunctions," J. Appl. Phys. **80**(8), 4411–4420 (1996).

[50] S. Chand and J. Kumar, "Current-voltage characteristics and barrier parameters of Pd$_2$Si/p- Si(111) Schottky diodes in a wide temperature range," Semicond. Sci. Technol. **10**, 1680 (1995).

[51] L. F. Marsal, I. Martin, J. Pallares, A. Orpella, and R. Alcubilla, "Annealing effects on the conduction mechanisms of p$^+$- amorphous- Si$_{0.8}$C$_{0.2}$: H/n- crystalline- Si diodes," J. Appl. Phys. **94**(4), 2622–2626 (2003).

[52] T. F. Schulze, L. Korte, E. Conrad, M. Schmidt, and B. Rech, "Electrical transport mechanisms in a-Si:H/c-Si heterojunction solar cells," J. Appl. Phys. **107**(2), 023711 (2010).

[53] E. Arslan, Ş. Altındal, S. Özçelik, and E. Ozbay, "Dislocation-governed current-transport mechanism in (Ni/Au)- AlGaN/AlN/GaN heterostructures," J. Appl. Phys. **105**(2), 023705 (2009).

[54] J. H. Werner and H. H. Güttler, "Barrier inhomogeneities at Schottky contacts," J. Appl. Phys. **69**(3), 1522–1533 (1991).

[55] J. H. Werner and H. H. Güttler, "Transport properties of inhomogeneous Schottky contacts," Phys. Scr. **T39**, 258–264 (1991).

[56] M. Isik, O. Surucu, and N. M. Gasanly, "Temperature-dependent current-voltage characteristics of p- GaSe$_{0.75}$S$_{0.25}$/n- Si heterojunction," Appl. Phys. A **129**(8), 538 (2023).

14 December 2024 12:01:40

Supplementary Materials

Capacitance characterization and current transport mechanism of ZnSnN$_2$ heterojunctions

Fan Ye[*], Zi-Cheng Zhao, Cang-Shuang He, Jian-Lin Liang, Qian Gao, Yi-Zhu Xie,

Dong-Ping Zhang, Xing-Min Cai[*]

Key Laboratory of Optoelectronic Devices and Systems of Ministry of Education and

Guangdong Province, Shenzhen Key Laboratory of Advanced Thin Films and

Applications, College of Physics and Optoelectronic Engineering, and

State Key Laboratory of Radio Frequency Heterogeneous Integration,

Shenzhen University, Shenzhen, 518060, China

Methods about preparing the Cu$_2$O\ZnSnN$_2$ heterojunctions

To fabricate Cu$_2$O\ZnSnN$_2$ heterojunctions (HJ), indium tin oxide-coated glasses (ITO, 6 Ω per square and 185 nm thick) were used as the substrates. Before film deposition, a mask with the same size as the ITO glass was placed on it. The mask has 9 square windows (3×3 cm^2) inside which thin films can be directly deposited on ITO. On the mask-covered ITO glass, Cu$_2$O was firstly deposited under exactly the same conditions as listed previously. When the substrates cooled down to room temperature (RT) naturally, ZnSnN$_2$ was secondly deposited under exactly the same conditions as listed previously. On the surface of ZnSnN$_2$, indium tin alloy is melted and pasted to

[*]Corresponding author, E-mail: yefan@szu.edu.cn; caixm@szu.edu.cn.

Note: The Reference in this Supplementary Materials follows that of the manuscript.

act as an Ohmic electrode and the $Cu_2O\backslash ZnSnN_2$ pn HJ with the structure of glass$\backslash$ITO$\backslash Cu_2O\backslash ZnSnN_2\backslash$InSn were fabricated.

Characterization methods of ZnSnN$_2$ and Cu$_2$O

Film samples deposited on K9 glass were structurally characterized with X-ray diffraction (XRD, D/max 2500 PC, 18 kW, Cu Kα radiation) and Raman scattering (XploRA PLUS Raman microscope, the laser wavelength is 532 nm). The film thickness was measured with a surface profiler (Veeco Dektak 3ST). The optical properties including the reflectance and transmittance of the samples were measured with an UV/VIS spectrophotometer (Perkin-Elmer, Lambda 900). The surface and cross-sectional morphologies of the samples deposited on silicon were measured with scanning electron microscopy (SEM, Supra 55 Sapphire). The electrical properties were measured with RT Hall effect (HL 5500 PC, Van der Pauw electrode was used and melted alloy of In and Sn was dropped at the four corners of a square sample to act as electrodes).

Characterizations of the photovoltaic properties of the HJ

The current I versus the applied voltage V (IV) curves of the $Cu_2O\backslash ZnSnN_2$ HJ were measured at RT with a multi-meter (Keithley, 2400 Series) under AM1.5 light illumination (which is from an AAA solar simulator with the intensity calibrated to be 100 mW/cm^2 through a Si reference cell). The external quantum efficiency (EQE)

measurement was measured with a solar cell QE/IPCE (incident photon to charge carrier efficiency) measurement instrument (Zolix, Solar Cell Scan - 100).

The XRD, Raman scattering and Tauc plots of ZnSnN$_2$ and Cu$_2$O

ZnSnN$_2$ together with Cu$_2$O were measured with XRD, Raman scattering and UV/VIS spectroscopy. The results are shown as Fig. **S1** in Supplementary Materials (S.M.) In Fig. **S1**(a), there are no diffraction peaks near 21° and so the prepared ZnSnN$_2$ is wurtzite with Zn and Sn randomly distributed on the cation sublattice.[15,16] The peaks in Fig.**S1** (b) are well-matched with those of simple cubic Cu$_2$O with no impurity peaks detected and with (111) as the preferred orientation.[33,35] No sharp Raman scattering peaks but 4 wide humps consistent with previous work[17] are observed (Fig.**S1** (c)). This is similar to its theoretical high-resolution phonon density of states spectrum.[18] This implies that ZnSnN$_2$ is phonon glass like with disorder in the cation sublattice and is in agreement with the XRD results. In Fig.**S1** (d), the Raman scattering peaks of Cu$_2$O at 217.5 cm^{-1}, 410.8 cm^{-1}, 515.1 cm^{-1} and 625.4 cm^{-1} are consistent with those reported in literature.[33,34] The relationship between transmittance T$_r$, reflectance R$_e$ and absorption coefficient α is that α is equal to $d^{-1} \times ln[(1 - R_e)/T_r]$, where d is the thickness of the film (d of ZnSnN$_2$ and Cu$_2$O are about 312 nm and 729 nm). For direct bandgap semiconductors, the relationship between α and optical bandgap E$_g$ is that $(\alpha h v)^2$ equals $A(hv\text{-}E_g)$, where A is a constant, h is the Planck constant and v is the photon frequency. From the $(\alpha h v)^2$ versus hv curves (Tauc plots) of ZnSnN$_2$ and Cu$_2$O (Fig.**S1** (e) and (f)), E$_g$ of ZnSnN$_2$ and Cu$_2$O

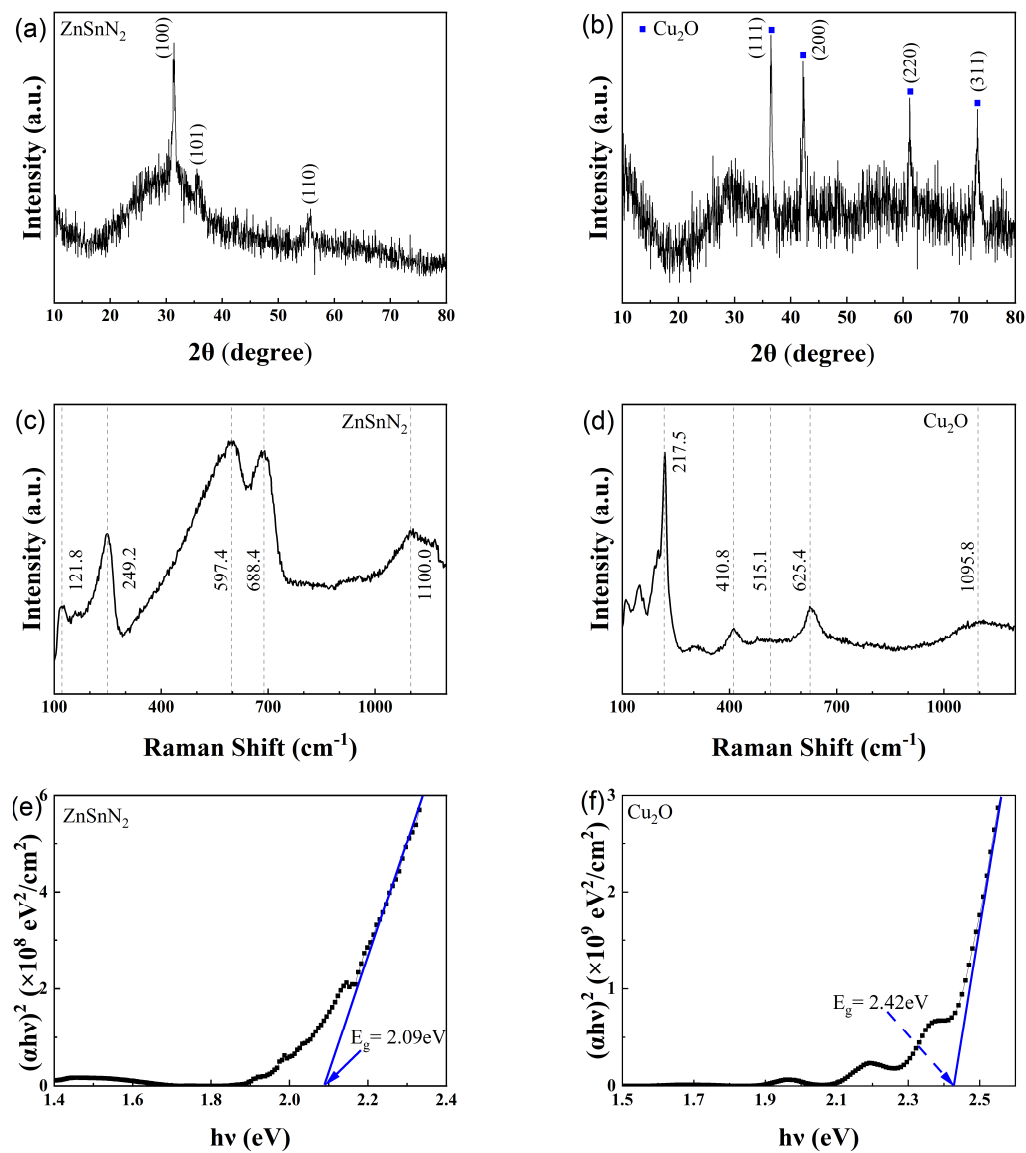are found to be 2.09 and 2.42 eV by extrapolating the linear region to intercept the $h\nu$ axis.

Fig. **S1**. XRD patterns of (a) $ZnSnN_2$ and (b) Cu_2O; Raman spectra of (c) $ZnSnN_2$ and (d) Cu_2O; Tauc plots of (e) $ZnSnN_2$ and (f) Cu_2O.

SEM images and Hall effect measurements

The SEM images of the samples are in Fig. **S2**, S.M.. In Fig. **S2**(a), it can be seen that the surface of $ZnSnN_2$ is dense with tiny grains observed. In Fig.**S2** (b), large

pyramid-like grains are observed from the surface of Cu_2O thin film and these rough pyramids possibly correspond to the (111) preferred orientation.[35] From the cross-sectional images of Fig.**S2** (c) and (d), it can be found that both grow in columns.
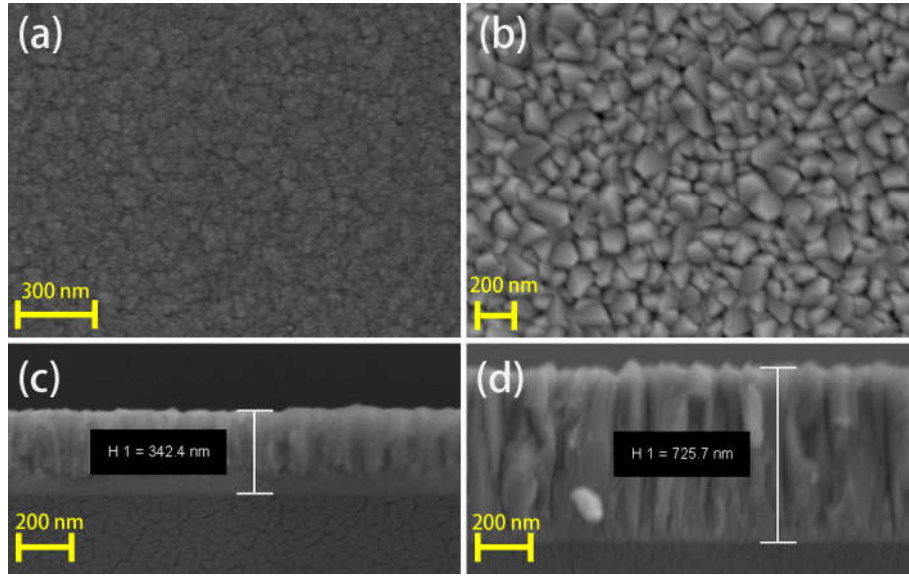

Fig. **S2**. Top view SEM images of (a) $ZnSnN_2$ and (b) Cu_2O; Cross-sectional SEM images of (c) $ZnSnN_2$ and (d) Cu_2O.

Hall effect measurement results shows that $ZnSnN_2$ is n-type conductive with electron density of 4.57×10^{16} cm^{-3}, mobility of 2.86 cm$^2\cdot$V$^{-1}\cdot$s^{-1} and resistivity of 47.69 ohm·cm. The electron density of $ZnSnN_2$ is much smaller than its RT density of states of the conduction band (1.04×10^{18} cm^{-3}), indicating that it is non-degenerate and the Fermi-level E_f is 0.08 eV below its conduction band minimum E_c.[27] Cu_2O is p-type conductive with hole density of 1.09×10^{15} cm^{-3}, mobility of 39.80 cm$^2\cdot$V$^{-1}\cdot$s^{-1} and resistivity of 144.40 ohm·cm.

Fig.**S3**(a) shows the JV curves of the $Cu_2O\backslash ZnSnN_2$ HJ illuminated under AM1.5G (the inset shows the cross sectional schematic of the HJ). The open circuit voltage V_{oc} and short circuit current density J_{sc} are 0.12 V and 0.29 mA/cm^2 while the fill factor (FF) and power conversion efficiency (PCE) are 33.07% and 0.012%. Fig.**S3**(b) shows the EQE spectrum of the HJ. There are two relatively steep slopes in the figure, the one at about 600 nm is the absorption edge of $ZnSnN_2$ while the steep slope at about 500 nm is the absorption edge of Cu_2O.[33] The $[E\times ln(1-EQE)]^2$ versus photon energy E plot (E=hc/λ with c and λ to be the speed and wavelength of the incident light) is also in Fig.**S3**(b). As it can be seen, the intercept of the linear extrapolation and the E axis is the optical bandgap of the device.[6] There are two obvious linear regions in the figure, and the extrapolated intercepts are about 2.07 and 2.45 eV, in agreement with the previously measured band gaps of $ZnSnN_2$ and Cu_2O.
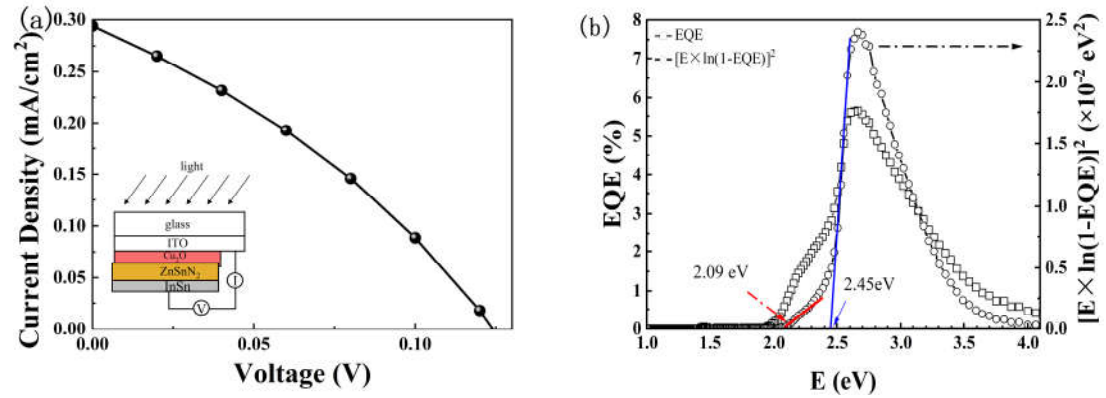

Fig.**S3** (a) The illuminated JV curve of the HJ (the inset shows its schematic structure); (b) EQE spectrum and $[E\times ln(1-EQE)]^2$ versus the photon energy E plot.
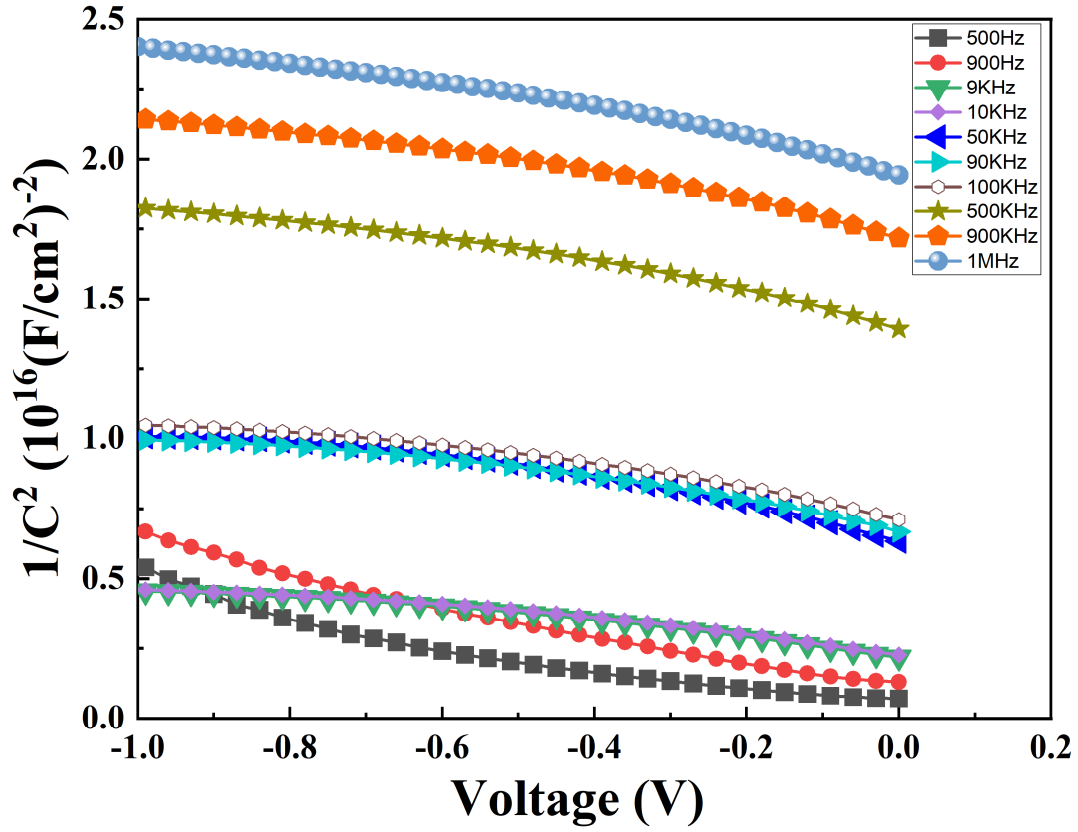
Fig. **S4.** The reverse-biased C^{-2} versus V curves measured at all the frequencies.

All the CV curves are fitted to $C = C_{SC}+C_{IS}= A_{sc}/(V_{bi}-V)^{1/2}+C_{IS}$, and the fitting parameters are A_{SC}, V_{bi} and C_{IS}. The fitting results are listed in Table **S1**. For 500 Hz and 900 Hz, the fitting shows that interface state capacitance C_{IS} is negative, implying that the fitting fails here at 500 Hz and 900 Hz.

Table **S1**. The fitting results of the CV curves. The fitting formula is $C = C_{SC}+C_{IS}= A_{sc}/(V_{bi}-V)^{1/2}+C_{IS}$ with A_{SC}, V_{bi} and C_{IS} as the fitting parameters.

f (Hz)	A_{SC} ($10^{-7}V^{0.5}\cdot F/cm^2$)	V_{bi} (V)	C_{IS} ($10^{-7}F/cm^2$)
500	0.6367	0.7588	-0.3433
900	0.2544	0.4572	-0.0889
9 K	0.0667	0.2678	0.0867
10 K	0.0622	0.2617	0.0900
50 K	0.0267	0.2623	0.0756
90 K	0.0267	0.3274	0.0767
100 K	0.0256	0.3335	0.0756
0.5 M	0.0167	0.4472	0.0600
0.9 M	0.0133	0.4806	0.0578
1 M	0.0144	0.5942	0.0533

The fitted C_{SC}^{-2} or $(C-C_{IS})^{-2}$ versus V curves at 100 kHz, 90 kHz, 50 kHz, 10 kHz and 9 kHz are still slightly curved due to deep energy levels or traps, as shown below in Fig.**S5**.
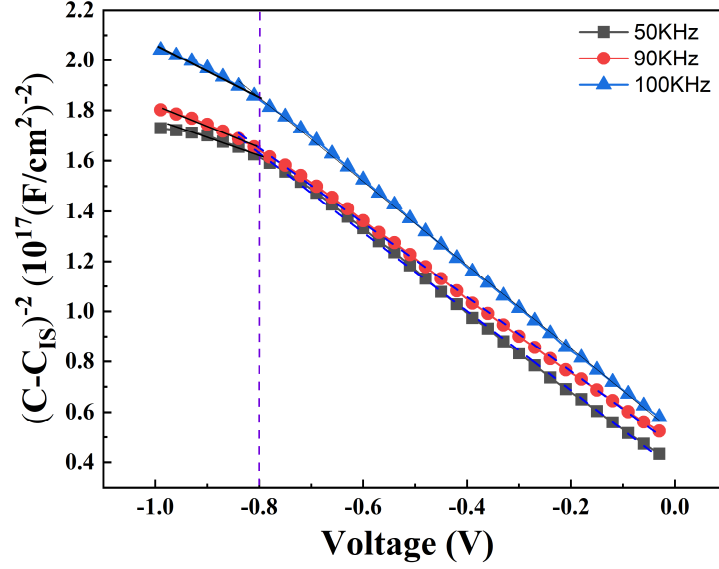
(a)The $(C-C_{IS})^{-2}$ versus V curves at 100 KHz, 90 KHz and 50 KHz;
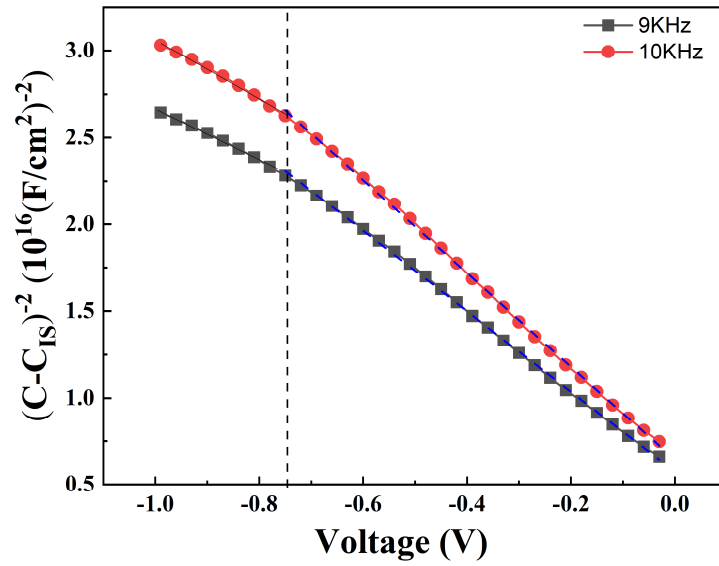
(b)The $(C-C_{IS})^{-2}$ versus V curves at 10 KHz and 9 KHz.

Fig. **S5** The $(C-C_{IS})^{-2}$ versus V curves.

Calculating[39-41] the energy levels and density of the traps from Fig. S5.

The energy level of the traps E_{DL} with respect to the conduction band bottom E_c is

$$E_c - E_{DL} = E_c - E_f + qV_{bi} - qV_{inf} \quad ,$$

where V_{inf} is the inflection point of the $(C-C_{IS})^{-2}$ versus V curves. From Fig.**S5**(a), it can be found that V_{inf}=-0.8 V for the curves at 100 KHz, 90 KHz and 50 KHz and E_c-E_{DL} is calculated to be 1.21, 1.21 and 1.14 eV for these curves (the corresponding V_{bi} from Table **S1**). For the curves at 10 KHz and 9 KHz (Fig.**S5** (b)), V_{inf}=-0.745 V and E_c-E_{DL} is calculated to be 1.09 eV for both (V_{bi} is also from Table **S1**).

From the slope of the linear section of the $(C-C_{IS})^{-2}$ versus V curves near zero-bias, the doping density of ZnSnN$_2$, N$_D$, can be calculated since $\frac{dC^{-2}}{dV} = \frac{2}{q\varepsilon_r\varepsilon_0}\frac{1}{N_D}$, while from the slope of the section after the inflection point, the density of deep energy levels N$_{DL}$ can be calculated since $\frac{dC^{-2}}{dV} = \frac{2}{q\varepsilon_r\varepsilon_0}\frac{1}{N_D+N_{DL}}$ at this range. The energy levels (E_c-E_{DL}) and their density (N$_{DL}$) are listed in Table **S2**. Three deep energy levels located at 1.21, 1.14 and 1.09 eV below E_c can be identified here.

Table **S2**. The deep energy levels E_c-E_{DL} and their density N$_{DL}$ calculated from Fig. **S5**.

f (Hz)	E_c-E_{DL} (eV)	N_{DL} (cm^{-3})
9 k	1.09	2.90×10^{14}
10 k	1.09	2.82×10^{14}
50 k	1.14	1.44×10^{14}
90 k	1.21	7.00×10^{13}
100 k	1.21	4.88×10^{13}

Table **S3**. The fitting results of the interface states capacitance C_{IS} based on the model of discrete energy levels ($C_{IS} = C_S + \sum_1^m C_{it-i}/[1 + (2\pi f \tau_i)^2]$) and the calculated density of interface states D_{it-i} and the interface states energy level E_c-E_{it-i} of the i-th level. When $C_S \neq 0$, C_S is fitted to be 5.60×10^{-9} F/cm^2.

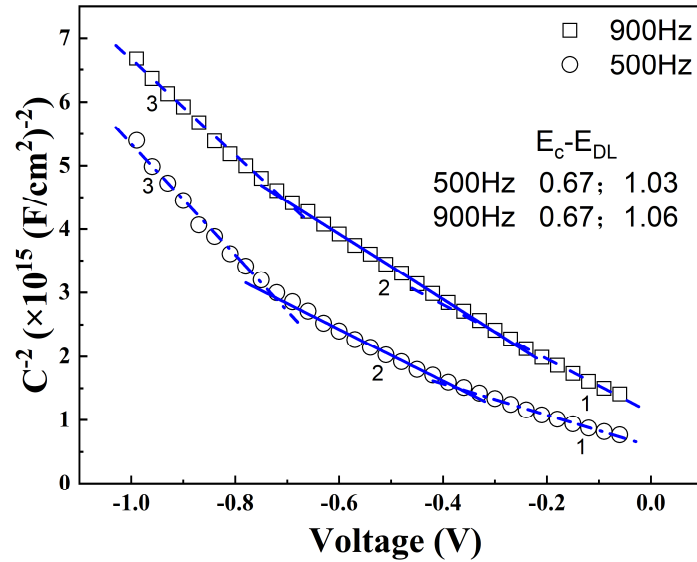|	C_S=0, m=1	C_S=0, m=2	$C_S \neq 0$, m=1
C_{it-1} (F/cm^2)	7.93×10^{-9}	2.42×10^{-9}	8.63×10^{-9}
τ_1 (s)	1.15×10^{-7}	1.77×10^{-6}	1.28×10^{-6}
D_{it-1} (states·eV^{-1}·cm^{-2})	4.95×10^{10}	1.51×10^{10}	5.39×10^{10}
E_c-E_{it-1} (eV)	-0.04	0.03	0.03
C_{it-2} (F/cm^2)	-	6.29×10^{-9}	-
τ_2 (s)	-	6.34×10^{-8}	-
D_{it-2} (states·eV^{-1}·cm^{-2})	-	3.93×10^{10}	-
E_c-E_{it-2} (eV)	-	-0.05	-

Fig. **S6** The C^{-2} versus V curves at 500 Hz and 900 Hz with 3 linear sections observed.

Calculating[46,47] the energy levels and density of the traps from Fig. S6

In Fig. **S6**, the C^{-2} versus V curves can be divided into 3 sections labeled as 1, 2 and 3. From section 1 and based on the assumption that the interface states are in equilibrium with ZnSnN$_2$, the doping density of ZnSnN$_2$, N$_D$ and the built-in potential, V$_{bi}$ can be calculated from the slope and horizontal intercept V$_{interc1}$ since the slope $(\frac{dC^{-2}}{dV})_1 = \frac{2}{q\varepsilon_r\varepsilon_0}\frac{1}{N_D(1+\alpha_{it})}$, $V_{interc1} = V_{bi}(1 + \alpha_{it})$,and $\alpha_{it} = \frac{qD_{it}\delta}{\varepsilon_r\varepsilon_0}$, where the density of interface states D$_{it}$=5.00×10^{10} states·eV^{-1}·cm^{-2} and δ=0.5 nm can be used.

The slope of section 2 is $(\frac{dC^{-2}}{dV})_2 = \frac{2}{q\varepsilon_r\varepsilon_0}\frac{N_D+N_{DL-s2}}{N_D{}^2}$ and its intercept $V_{interc2} = V_{bi} - \frac{E_f-E_{DL-s2}}{q}\frac{N_{DL-s2}}{N_D+N_{DL-s2}}$ where N$_{DL-s2}$ is the density of the trap while E$_f$-E$_{DL-s2}$ is the energy gap between E$_f$ and the energy level E$_{DL-s2}$ of the trap corresponding to this section. Therefore, E$_c$-E$_{DL-s2}$= (E$_c$-E$_f$)+(E$_f$-E$_{DL-s2}$)=0.08+(E$_f$-E$_{DL-s2}$).

The slope of section 3 is $(\frac{dC^{-2}}{dV})_3 = \frac{2}{q\varepsilon_r\varepsilon_0}\frac{N_D+N_{DL-s2}+N_{DL-s3}}{N_D{}^2}$ and its intercept $V_{interc3} = V_{bi} - \frac{(E_f-E_{DL-s2})N_{DL-s2}+(E_f-E_{DL-s3})N_{DL-s3}}{q(N_D+N_{DL-s2}+N_{DL-s3})}$ where N$_{DL-s3}$ is the density of the trap levels while E$_f$-E$_{DL-s3}$ is the energy gap between E$_f$ and the energy level E$_{DL-s3}$ of the trap related to this section. E$_c$-E$_{DL-s3}$= (E$_c$-E$_f$)+(E$_f$-E$_{DL-s3}$)=0.08+(E$_f$-E$_{DL-s3}$).

With D$_{it}$=5.00×10^{10} states·eV^{-1}·cm^{-2} and δ=0.5 nm, α$_{it}$ is calculated to be 4.52× 10^{-4}. From section 1 of the C^{-2} versus V curve at 500 Hz, V$_{bi}$ and N$_D$ are calculated to be 0.25 V and 5.37×10^{15} cm^{-3}. From section 2 of this curve, E$_f$-E$_{DL-s2}$ (E$_c$-E$_{DL-s2}$) and N$_{DL-s2}$ are calculated to be 0.59 eV (0.67 eV) and 3.25×10^{15} cm^{-3}. From section 3 of this curve, E$_f$-E$_{DL-s3}$ (E$_c$-E$_{DL-s3}$) and N$_{DL-s3}$ are calculated to be 0.95 eV (1.03 eV) and 1.03×10^{16} cm^{-3}.

From section 1 of the C^{-2} versus V curve at 900 Hz, V$_{bi}$ and N$_D$ are calculated to be 0.25 V and 2.96×10^{15} cm^{-3}. From section 2 of this curve, E$_f$-E$_{DL-s2}$ (E$_c$-E$_{DL-s2}$) and

N_{DL-s2} are calculated to be 0.59 eV (0.67 eV) and 5.91×10^{14} cm^{-3}. From section 3 of this curve, E_f-E_{DL-s3} (E_c-E_{DL-s3}) and N_{DL-s3} are calculated to be 0.98 eV (1.06 eV) and 1.66×10^{15} cm^{-3}.

Table **S4**. The calculating results based on Fig.**S6**.

f (Hz)	Section 1		Section 2			Section 3		
	V_{bi} (V)	N_D (cm^{-3})	E_f-E_{DL-s2} (eV)	E_c-E_{DL-s2} (eV)	N_{DL-s2} (cm^{-3})	E_f-E_{DL-s3} (eV)	E_c-E_{DL-s3} (eV)	N_{DL-s3} (cm^{-3})
500	0.25	5.37×10^{15}	0.59	0.67	3.25×10^{15}	0.95	1.03	1.03×10^{16}
900	0.25	2.96×10^{15}	0.59	0.67	5.91×10^{14}	0.98	1.06	1.66×10^{15}

Calculating N_{CV} and N_{DLCP}

For drive level capacitance, the capacitance was obtained at each frequency with the maximum direct current (DC) bias from -0.25 to 0V while the alternative current amplitude is from 0.015 to 0.135 V. At each maximum bias, the capacitance versus the direct current voltage can be obtained and C_0 and C_1 can be fitted. The charge density N_{DLCP} is calculated[48] as follows: $N_{DLCP} = -\frac{C_0^3}{2q\varepsilon_0\varepsilon_r S_j^2 C_1}$, where q is the elementary charge, ε_0 is the vacuum permittivity, ε_r is the relative dielectric constant of ZnSnN$_2$ (ε_r =11[14]), S_j is the junction area (0.09 cm^2 here). The depth $\langle x \rangle$ corresponding to N_{DLCP} is $\langle x \rangle = \frac{\varepsilon_0\varepsilon_r S_j}{C_0}$. For the CV curves measured at each frequency, the charge density $N_{CV} = \frac{C^3}{q\varepsilon_0\varepsilon_r S_j^2}(\frac{dC}{dV})^{-1}$ and the depth $\langle x \rangle = \frac{\varepsilon_0\varepsilon_r S_j}{C}$. Both N_{DLCP} and N_{CV} are in Fig.**S7**. The zero bias difference $N_{CV}-N_{DLCP}$ is used as the total interface states N_{it}.
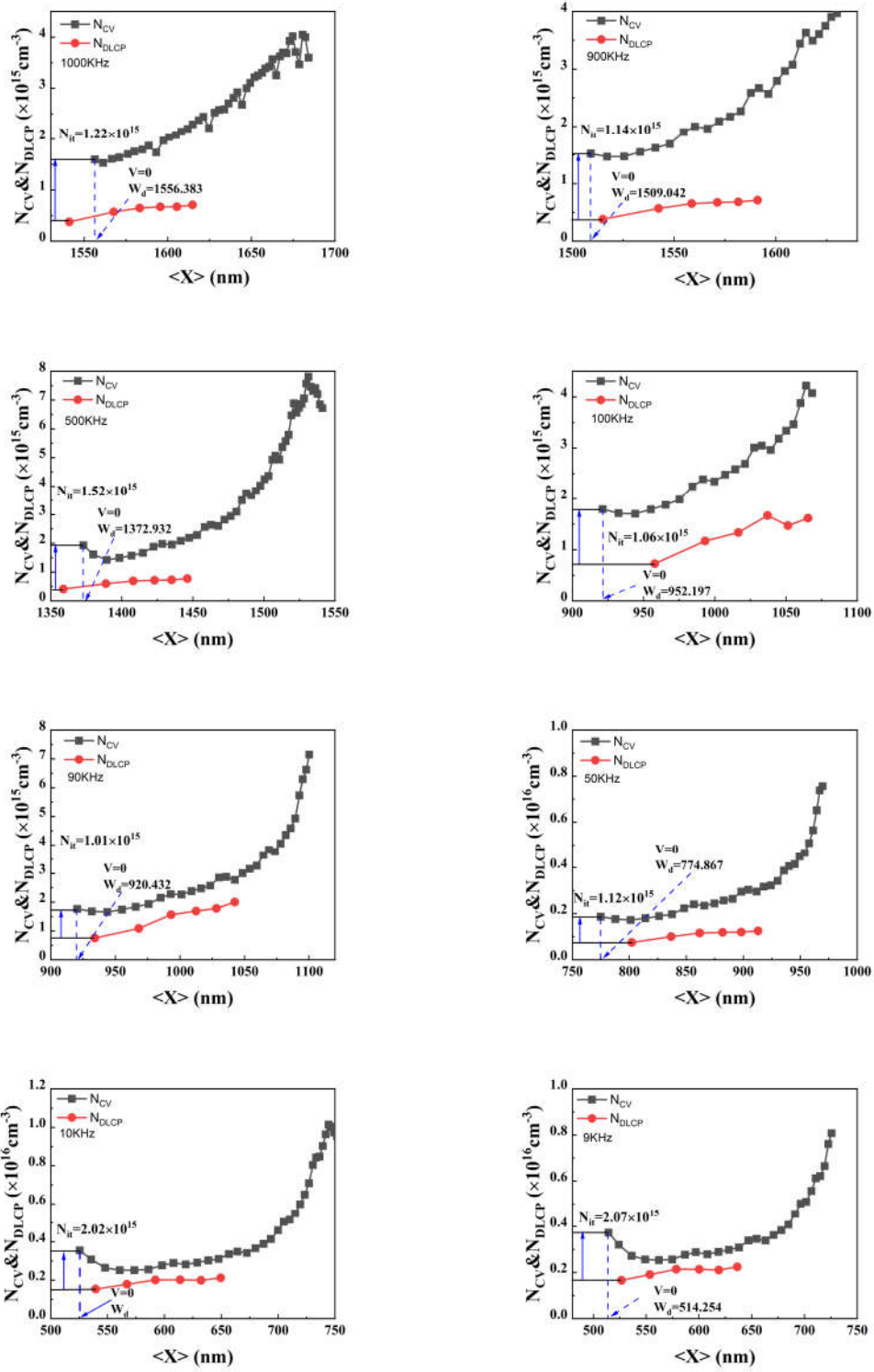
Fig. **S7** The depth profile of the charge density N$_{CV}$ and N$_{DLCP}$. N$_{CV}$ is calculated from the CV curves measured at different frequency while N$_{DLCP}$ is from drive-level capacitance.